Journal of CO2 Utilization 110 (2026) 103516

Contents lists available at ScienceDirect

Journal of CO2 Utilization

journal homepage: www.elsevier.com/locate/jcou

# Development of hierarchical UiO-66/ZIF-8/ZIF-67 hybrid composites for enhanced $CO_2$ adsorption at varying temperatures and pressures

Zineb Ouzrour [a], Hicham Akaya [a], Soukaina Lamnini [a], Katalin Balázsi [b], Zsolt Czigány [b], Tausif Altamash [a,*], Johan Jacquemin [a,*]

[a] College of Chemical Sciences and Engineering (CCSE), Department of Materials Science, Energy and Nano-Engineering (MSN), Mohammed VI Polytechnic University (UM6P), Benguerir 43150, Morocco

[b] HUN-REN Centre for Energy Research, Institute of Technical Physics and Materials Science, P.O. Box 49, Budapest H-1525, Hungary

ARTICLE INFO

*Keywords:*
Metal-organic frameworks (MOFs)
Zeolitic imidazolate frameworks (ZIFs)
Composite materials
$CO_2$ adsorption
High-pressure gas capture

ABSTRACT

We developed a simple method to create hybrid metal-organic framework (MOF) composites to improve $CO_2$ adsorption performance: ZIF-8&ZIF-67 (ZZ), UiO-66&ZIF-8 (UZ), and UiO-66&ZIF-8&ZIF-67 (ZUZ). We conducted structural and morphological characterization using TEM, XRD, FTIR, and EDS to confirm the successful formation of the composites. $N_2$ sorption analysis showed a significant increase in BET surface area. The surface area increased from 582.84 $m^2.g^{-1}$ for neat UiO-66–1672.52 $m^2.g^{-1}$ for UZ, with ZUZ also showing a high surface area of 1169.79 $m^2.g^{-1}$. We carried out $CO_2$ adsorption measurements at 273, 303, and 313 K under different pressures. At 303 K, ZUZ showed higher $CO_2$ uptake, reaching 1.5 mmol/g at 1 bar and 7.0 mmol/g at 10 bars. In contrast, neat UiO-66 only reached 1.2 mmol/g and 3.2 mmol/g under the same conditions. These results highlight how structural hybridization can change porosity and improve $CO_2$ adsorption performance.

## 1. Introduction

In the past decades, rising atmospheric $CO_2$ levels driven by anthropogenic activities have sped up research in a multidirectional way, with an assessment into porous and recyclable liquid materials as sustainable alternatives to conventional amine-based absorption technologies [1,2]. Unlike chemical absorption in amine solutions, which involves chemisorption through strong covalent or ionic adsorbate-adsorbent bonds requiring substantial thermal energy for regeneration, gas adsorption in metal-organic frameworks (MOFs) proceeds predominantly via reversible physisorption mechanisms[3,4]. These physisorptive interactions, characterized by weak van der Waals forces and electrostatic attractions, significantly reduce energy regeneration requirements, reduce operational costs, and improve framework stability across multiple adsorption-desorption cycles.

ZIFs are a subclass of MOFs because they have shared common properties [5]. Structurally, ZIFs are formed by coordinating metal ions with imidazole-based ligands. Two extensively studied ZIFs for $CO_2$ capture are ZIF-8 and ZIF-67, synthesized from zinc ions and cobalt ions, respectively [6,7]. Owing to their unique structural properties ZIF-8 and ZIF-67 offer high surface area and tunable porosity. Additionally, they exhibit good thermal and chemical stability, making them suitable for use across a wide range of conditions [8,9]. Both ZIFs share the same sodalite-type topology but differ in their metal centers: $Zn^{2+}$ in ZIF-8 confers high thermal and chemical stability, while $Co^{2+}$ in ZIF-67 enables stronger $CO_2$ interactions via Lewis acid-base affinity, thereby enhancing adsorption capacity and selectivity[10].

The MOF UiO-66, which has gained significant attention for $CO_2$ capture, is composed of zirconium ions coordinated with terephthalic acid linkers. UiO-66 contains a high surface area (800-1200 $m^2.g^{-1}$) and porosity [11]. However, challenges arise from hydrophilicity, where competitive water adsorption reduces $CO_2$ uptake capacity under humid conditions. Such a limitation creates an unwanted issue when quantifying $CO_2$ capture scenarios, particularly in post-combustion flue gas streams with a substantial moisture content [12].

Our approach involves straightforward synthesis of a complex structure to create hybrid composite structures through forward reactions, specifically with ZIF-8&ZIF-67 (ZZ), UiO-66&ZIF-8 (UZ), and ZIF-8&UiO-66&ZIF-67 (ZUZ), designed to integrate hydrophobic stability with enhanced $CO_2$ affinity. The ZUZ composite synergistically combines the hydrophobic characteristics of ZIF-8, the strong $CO_2$ interaction arising from $Co^{2+}$ sites in ZIF-67, and the high porosity of

* Corresponding authors.
*E-mail addresses:* tausif.altamash@um6p.ma (T. Altamash), johan.jacquemin@um6p.ma (J. Jacquemin).

https://doi.org/10.1016/j.jcou.2026.103516
Received 4 February 2026; Received in revised form 5 June 2026; Accepted 2 July 2026

UiO-66, resulting in superior adsorption performance under high-pressure conditions [13-17].

To evaluate $CO_2$ adsorption in the hybrid composites, experiments were carried out at different temperatures and pressures, followed by characterization and thermal analysis. Furthermore, the experimental data were analyzed using the Langmuir, Freundlich, and Temkin isotherm models, which helped in evaluating the monolayer capacity, surface heterogeneity, micropore filling, and adsorption energy variation. Among these models, the Freundlich model exhibited the best fit for ZUZ and ZZ, indicating heterogeneous surface adsorption as the dominant mechanism. While for our UZ and UiO-66, the Langmuir model provided a better fit, suggesting that $CO_2$ adsorption on these materials is mainly governed by monolayer adsorption. The thermodynamic analysis of $CO_2$ adsorption on ZUZ reveals a spontaneous and exothermic physisorption process with $\Delta G^{\circ}$=-1622.64, -992.71, and -534.47 J/mol at 273, 303, and 313 K, respectively. The negative enthalpy change $\Delta H^{\circ}$ = -1035.9 J/mol confirms that the adsorption process is dominated by physisorption, indicating that $CO_2$ uptake on ZUZ is suitable for low-energy regeneration. To the best of our knowledge and approach, the design of a triple-MOF composite integrating two distinct ZIF topologies with UiO-66, using PVP as a capping agent, has not been previously reported elsewhere; therefore, we have attempted to present a systematic report.

Teller (BET) method within the relative pressure range (typically P/$P_0$=0.05-1) appropriate for mesoporous and microporous materials. This technique provides critical insights into the textural properties of porous materials and is widely used to characterize metal-organic frameworks [17].

## 2. Materials and methods

### 2.1. Materials

All chemicals were purchased from commercial sources (Sigma Aldrich) and used without further purification unless otherwise noted. Zirconium oxychloride octahydrate ($ZrOCl_2{\cdot}8\ H_2O$, >98%), terephthalic acid ($H_2BDC$, >99%), N, N-dimethylformamide (DMF, >99.8%), hydrochloric acid (HCl, 37%), zinc nitrate hexahydrate ($Zn(NO_3)_2{\cdot}6\ H_2O$, > 98%), cobalt nitrate hexahydrate ($Co(NO_3)_2{\cdot}6\ H_2O$, > 98%), 2-methylimidazole (2-MIM, >99%), Methanol (MeOH, >98%), and polyvinylpyrrolidone (PVP, MW= 40,000).

### 2.2. Synthesis

#### 2.2.1. Preparation of UiO−66

The synthesis of UiO−66 followed a similar protocol reported elsewhere [12]. In total, a 100 mL glass vial was charged with $ZrOCl_2{\cdot}8\ H_2O$ (483 mg), dissolved in DMF (10 mL), and HCl (1 mL, 37%). The mixture was sonicated for 20 min to ensure complete dissolution. In a separate 100 mL vial, terephthalic acid (249 mg) was dissolved in DMF (20 mL) and sonicated for 10 min. The terephthalic acid solution was transferred to the first vial, and the combined mixture was sonicated for an additional 20 min. The reaction mixture was heated in a programmable oven at 120°C for 24 h. After cooling to room temperature, the white crystalline product was collected by centrifugation and washed sequentially with DMF (3 × 30 mL) and ethanol (3 × 30 mL) to remove unreacted organic linkers. The final product was dried in an oven at 60 °C for 24 h. Yield: 86.7% (360 mg). This yield is low compared to the literature, since the integration of HCl in the synthesis of UiO−66 introduces defects within the framework, such as missing-linker defects and unreacted sites in Zr clusters, which influence the yield of the material [16,18].

The synthetic route leading to the formation of UZ, ZZ, and ZUZ materials is depicted in Fig. 1.

#### 2.2.2. Preparation of ZIF−8

ZIF−8 was synthesized following this procedure with minor modification.

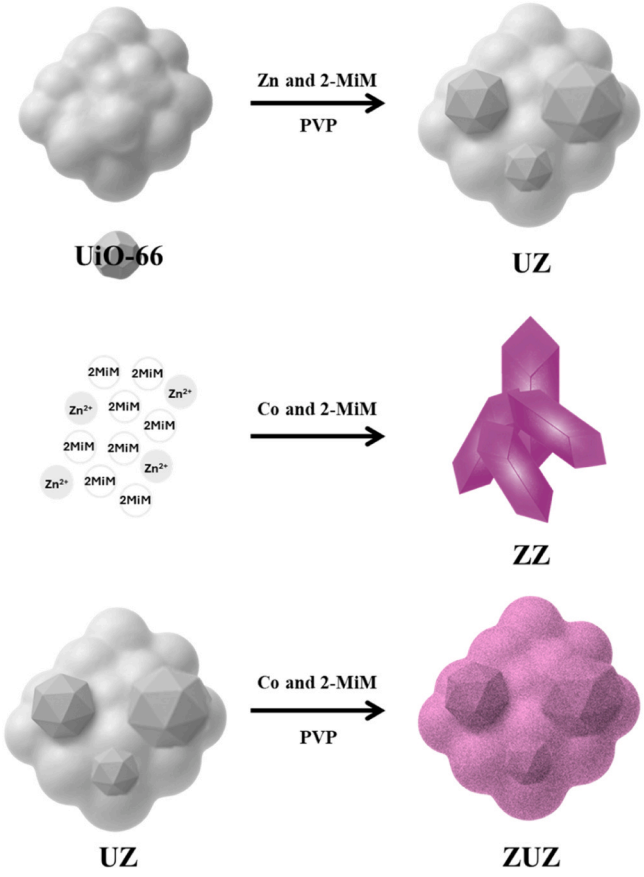


**Fig. 1.** Schematic representation of the stepwise synthesis procedures for the preparation of UiO−66-composites.

[19]. Zn $(NO_3)_2{\cdot}6\ H_2O$ (2.98 g) was dissolved in the suspension and stirred for an additional 12 h. A solution of 2-methylimidazole (2-MIM, 6.57 g) in absolute methanol (15 mL) was prepared and added to the suspension. The reaction mixture was stirred for 1 h at room temperature, and the product was collected by centrifugation and dried at 60 °C for 24 h. Yield: 71%.

#### 2.2.3. Preparation of ZIF−67

$Co(NO_3)2{\cdot}6\ H_2O$ (2.91 g) was dissolved in absolute methanol and stirred for 12 h. Then, a solution of 2-MIM (6.57 g, 80 mmol) in absolute methanol (15 mL) was added, and the mixture was stirred for 1 h. The resulting suspension was then further stirred for an additional hour, after which the product was collected by centrifugation and dried at 60 °C for 24 h, affording the product in 74% yield [20].

#### 2.2.4. Preparation of ZIF−8&UiO−66(UZ)

Following a recently modified procedure by Zhang et al. [21], UiO−66 (0.1 g) was dispersed in absolute methanol (35 mL) and sonicated at room temperature for an hour to obtain a homogeneous suspension. PVP (0.2 g) was added as a structure-directing agent [22], and the mixture was stirred continuously. After keeping for 12 h, Zn $(NO_3)_2{\cdot}6\ H_2O$ (2.98 g) was dissolved in the suspension and stirred for an additional 12 h. A solution of 2-methylimidazole (2-MIM, 6.57 g) in absolute methanol (15 mL) was prepared and added to the suspension. The reaction mixture was stirred for 1 h at room temperature, and the product was collected by centrifugation and dried at 60 °C for 24 h. Yield: 90%.

#### 2.2.5. Preparation of ZIF−8&ZIF−67 (ZZ)

Zn $(NO_3)_2{\cdot}6\ H_2O$ (2.98 g) was dissolved in absolute methanol and

stirred for 12 h. A solution of 2-MIM (6.57 g, 80 mmol) in absolute methanol (15 mL) was added, and the mixture was stirred for 1 h. Co $(NO_3)_2{\cdot}6\ H_2O$ (2.91 g) was then added to the suspension under continuous stirring for an additional hour. The product was collected by centrifugation and dried at 60 °C for 24 h, as reported according to the reference [23], reaching a yield of 75%.

#### 2.2.6. Preparation of ZIF−8&UiO−66&ZIF−67 (ZUZ)

UiO−66 (0.1 g) was dispersed in absolute methanol (35 mL) via sonication at 25 °C for 1 h to achieve a homogeneous suspension. PVP (0.2 g) was added as a capping agent [22], and the mixture was stirred continuously. After 12 h, Zn $(NO_3)_2{\cdot}6\ H_2O$ (2.98 g) was dissolved in the suspension and stirred for an additional 12 h. A solution of 2-MIM (6.57 g, 80 mmol) in absolute methanol (15 mL) was added, followed by 1 h of stirring. Finally, Co $(NO_3)_2{\cdot}6\ H_2O$ (2.91 g) was added, and the mixture was stirred for an additional hour before the product was collected by centrifugation and dried at 60 °C for 24 h, resulting in a yield of approximately 81%.

## 3. Characterization and measurements

### 3.1. Thermogravimetric analysis (TGA)

Thermal resistance and degradation characteristics were evaluated using a Discovery TGA thermogravimetric analyzer (TA Instruments, New Castle, DE, United States) following established protocols [24]. Sample masses of 10 mg were weighed using an analytical balance (accuracy ±0.1 mg) and placed in alumina crucibles. Samples were heated in a high-purity nitrogen atmosphere (99.99%, flow rate: 10 mL/min) from ambient temperature (25 ± 2 °C) to 700°C at a heating rate of 10 °C/min, with temperature calibration performed using high-purity metal standards following the guidelines [25]. Mass loss values were recorded continuously throughout the experiment, and derivative thermogravimetric curves were calculated to identify specific transition stages [26].

### 3.2. Fourier transform infrared (FTIR)

FTIR was performed to analyze the chemical composition using a PerkinElmer FTIR spectrometer equipped with a diamond ATR accessory. Before the analysis, background spectra were collected and automatically subtracted from sample spectra. Spectra were recorded in the range of 4000–600 $cm^{-1}$ with a resolution of 4 $cm^{-1}$, accumulating 16 scans per sample to improve signal-to-noise ratio. Data processing and peak analysis were performed using PerkinElmer Spectrum software (PerkinElmer Spectrum 10™ software) following already established procedures for spectral characterization and triplicated to ensure reproducibility, and thus averaged spectra are presented [27].

### 3.3. X-ray diffraction (XRD)

XRD was conducted to examine the crystalline structure using a D8 Advance Phaser diffractometer (Bruker D8 Advance) with CuKα radiation (λ = 1.54056 Å), following standard procedures for characterization [28]. Powdered samples were carefully ground using an agate mortar and pestle to ensure a uniform particle-size distribution and loaded onto zero-background silicon holders. Analyses were performed within a 2θ range of 5–60 ° at operating conditions of 40 kV and 40 mA, with a step size of 0.02 ° and a counting time of 1 s per step.

### 3.4. Transmission electron microscopy (TEM) and scanning transmission electron microscopy (STEM)

TEM and STEM were conducted on a Cs-corrected 200 kV Themis (Thermo Fisher) microscope with 0.8 Å resolution (in TEM mode) and equipped with *Energy Dispersive X-ray Spectroscopy (EDS)*. The TEM samples were made by dropping the dry powder on carbon-coated TEM grids (Ted Pella).

### 3.5. $N_2$ adsorption isotherms

$N_2$ isotherms were measured at 77 K using a Micromeritics TRISTAR II PLUS surface area and porosity analyzer. Before the measurements, the samples were degassed under vacuum at 120 °C for 12 h to remove any adsorbed moisture or residual solvents, ensuring accurate surface area analysis. The specific surface area was calculated using the Brunauer-Emmett-Teller (BET) method within the relative pressure range (typically $P/P_0$=0.05–1) appropriate for mesoporous and microporous materials. This technique provides critical insights into the textural properties of porous materials and is widely used to characterize metal-organic frameworks [17].

### 3.6. $CO_2$ adsorption-desorption

Adsorption isotherms of pure $CO_2$ for the tested samples were obtained using a SETARAM Gaspro GA apparatus maintained at isothermal conditions (T = 20 °C ± 0.1 °C) across a pressure gradient of 0–10 bar. Before experimentation, 0.1–0.12 g of sorbent was introduced into the equilibrium cell, with precise mass determination conducted before and after each measurement series to account for potential mass loss following activation. The cell volume containing the activated sample was calibrated using helium gas before degassing [29]. Two sequential pVT measurements were then performed to quantify: (i) the initial $CO_2$ gas phase concentration before interaction with the activated material, and (ii) the $CO_2$ gas phase concentration after achieving thermodynamic equilibrium under specific conditions. The differential between these measurements was adjusted for any thermal fluctuations, which provide a precise quantity (mmol) of $CO_2$ adsorbed or desorbed by the material [27]. All experimental procedures were conducted under strictly controlled isothermal conditions within an isochoric system, with sorption kinetics monitored via pressure variations (bar) as a function of time (s) until equilibrium was established (p = constant). For adsorption studies, sequential pressure increments were implemented by introducing precisely measured quantities of pure $CO_2$ (ΔP = 0.5 bar) into the equilibrium cell until the maximum absolute pressure reached 10 bar. Equally, the adsorption-desorption cycles were measured by following the procedure explained elsewhere [30,31].

### 3.7. Adsorption modeling

#### 3.7.1. Langmuir isotherm

The Langmuir model assumes that adsorption occurs on a homogeneous surface with a finite number of identical sites, and once a site is occupied, no further adsorption occurs. It also assumes there is no interaction between adsorbed molecules. Therefore, the adsorption follows a dynamic equilibrium between adsorbed and desorbed molecules [32].

$$qe = \frac{\text{qmax.KL.Pe}}{1 + \text{KL.Pe}}$$

.

$q_e$ = amount of gas adsorbed per unit mass of adsorbent (mmol/g).
$q_{max}$ = maximum adsorption capacity (mmol/g).
$K_L$ = Langmuir equilibrium constant (1/bar).
$P_e$ = equilibrium pressure of the adsorbate (bar).

#### 3.7.2. Freundlich isotherm

The Freundlich model is an empirical equation that assumes adsorption occurs on a heterogeneous surface with varying adsorption sites and multilayer adsorption. The adsorption energy decreases logarithmically as coverage increases [32].

$q_e = K_F P e^{(1/n)}$.
$q_e$ = amount of gas adsorbed per unit mass of adsorbent (mmol/g).
$K_F$ = Freundlich equilibrium constant (mmol/g) (bar$^{-1/n}$).
$P_e$ = equilibrium pressure of the adsorbate (bar).
n = adsorption intensity constant (dimensionless).

### 3.7.3. Temkin isotherm

The Temkin model assumes that adsorption heat decreases linearly with coverage due to adsorbate-adsorbate interactions [33].

$$q_e = B_T.\ln(A.Pe)$$

With

$$B_T = \frac{RT}{b}$$

where:
A = Temkin isotherm equilibrium binding constant (L/g).
b = Temkin adsorption heat constant (J/mol).
R = universal gas constant (8.314 J/mol·K).
T = absolute temperature (K).
Pe = equilibrium pressure (bar).

### 3.7.4. $CO_2$ adsorption thermodynamic analysis

The Gibbs free energy change (ΔG°) indicates spontaneity. A negative ΔG° value implies that the adsorption process is spontaneous under the given conditions, whereas a positive value suggests non-spontaneity. In this study, ΔG° was calculated at each temperature using the following relation:

$$\mathbf{\Delta G^\circ = \Delta H^\circ - T\Delta S^\circ = \quad -R.T.Ln(K_F)}$$

where R is the universal gas constant (8.314 J/mol·K), T is the temperature in Kelvin, and K represents the adsorption equilibrium constant derived from either the Langmuir or the Freundlich isotherm model, depending on the best fit. It should be noted that prior to the thermodynamic calculation, the Freundlich constant $K_F$ was the parameter used to compute ΔG° [34].

The enthalpy (ΔH°) and entropy (ΔS°) changes were determined from the linear form of the van't Hoff equation, which relates the temperature dependence of the equilibrium constant:

$$\mathbf{ln(K_F) = -\frac{\Delta H^\circ}{RT} + \frac{\Delta S^\circ}{R}}$$

.

A linear plot of lnK versus 1/T was used to extract ΔH° from the slope and ΔS° from the intercept. This method allows for the simultaneous determination of both parameters based on experimental equilibrium data across multiple temperatures [35].

## 4. Results and discussion

### 4.1. Composite morphology and phase

The XRD patterns of the synthesized sorbents UZ, ZZ and ZUZ as well as UiO−66 pristine are presented in Fig. 2. The presence of intense peaks at 2θ = 7.20°, 8.38°, 11.94° and 16.90° corresponding to planes of (111), (200), (220), and (311) respectively of the face-centered cubic UiO−66 structure (space group Fm-3m) confirm the high crystallinity and phase purity of the synthesized UiO−66 framework [36,37]. The presence of these peaks in composite materials indicates the retention of UiO−66's crystalline structure upon integration with other MOFs.

As ZIF−8 and ZIF−67. The diffraction pattern of ZIF−8 shows characteristic peaks at approximately 7.4°, 10.4°, 12.7°, 14.7°, 16.4°, and 18.0° of 2θ which correspond to the crystallographic planes (011), (002), (112), (022), (013), and (222) respectively. Similarly, ZIF−67

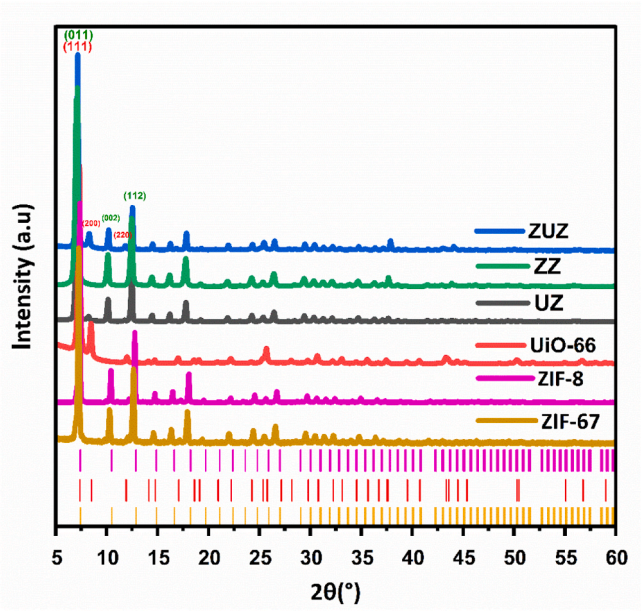


**Fig. 2.** XRD patterns of normalized UiO−66, ZZ, UZ, and ZUZ evidencing phase resemblance and the preservation of the MOFs structural integrity after. (COD ZIF−8: 4118891/COD UiO−66: 4512074/COD ZIF−67: 7247762).

shows diffraction peaks at nearly the same *2θ* values, associated to the same set of planes: (011), (002), (112), (022), (013), and (222) which planes in the cubic space group I-43m. Because both ZIFs share the same sodalite (SOD) topology, their diffraction peaks appear in overlapping positions [38].

The XRD pattern of the UZ composite containing ZIF−8 and UiO−66 shows reflections corresponding to both starting materials, confirming the coexistence of both frameworks within the hybrid structure. The well-defined peaks and absence of new diffraction signals suggest no significant structural preference or formation of an amorphous phase, confirming the successful synthesis of the UZ composite. In contrast, the XRD pattern of ZZ (ZIF−8&ZIF−67 composite) exhibits peaks that are characteristic of ZIF−8 and ZIF−67, while the absence of UiO−66-related peaks, particularly (200) and (220) at 8.38°and 11.94° confirms that this composite does not contain any UiO−66. The preserved sodalite topology of ZIF−8 and ZIF−67 is consistent with previous observations reported by Nazir et al. [39], who demonstrated that bimetallic ZIFs maintain the crystalline structure of their single-metal counterparts due to their analogous lattice parameters, atomic radii, and bond lengths. This structural similarity facilitates the unrestricted solubility of Zn within the Co-based ZIF, ensuring phase homogeneity and crystalline integrity. The ZUZ composite, which integrates UiO−66, ZIF−8, and ZIF−67, exhibits an XRD pattern that combines the reflections of both UZ and ZZ. The coexistence of UiO−66's characteristic peaks alongside those of ZIF−8 and ZIF−67 confirms the successful synthesis of a well-defined composite hybrid MOF structure. The absence of unidentified peaks suggests that the material is free from crystalline impurities or byproducts. These observations strongly support the hypothesis that UiO−66, ZIF−8, and ZIF−67 serve as part of ZUZ [39]. This configuration is particularly significant because it implies that the structural framework of UiO−66 remains intact, while the surface modifications with ZIFs contribute additional functional properties [39].

Fig. 3.**a** and **b** represent TGA curves and their derivatives of the synthesized composites. The TGA and DTA curves of UiO−66 show an initial slight weight loss in the temperature range of 30–120 °C, which is primarily caused by the evaporation of physical water, moisture, and adsorbed gases. Further weight loss of 18% and 34% was noticed in the ranges of 100–350 °C and 350–600 °C, respectively. These losses are linked to the degradation of the modulator (DMF), followed by

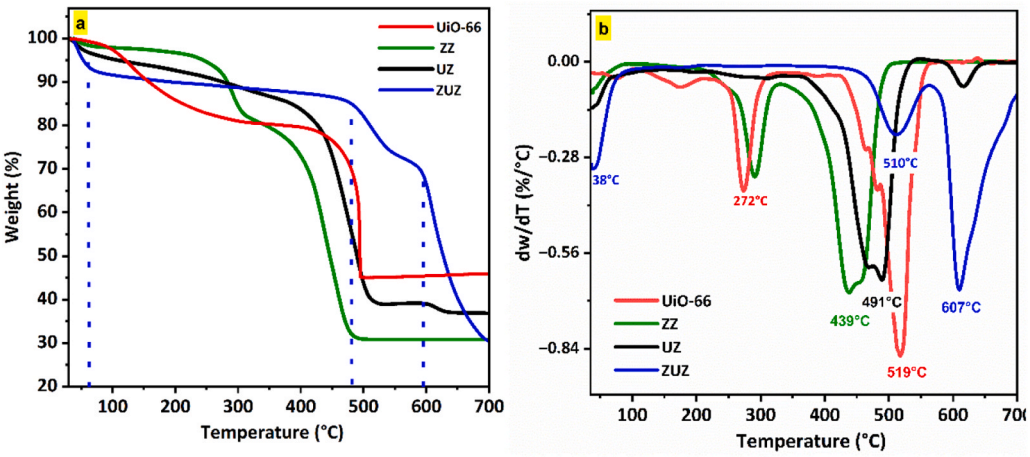


**Fig. 3.** (a) Thermogravimetric analysis and (b) derivative thermogravimetric curves highlighting their thermal stability, decomposition behavior, and framework integrity under elevated temperatures for UiO−66, ZZ, UZ and ZUZ.

degradation of the organic linkers 1,4-benzenedicarboxylate, leading to the formation of zirconium oxide ($ZrO_2$) [40]. The addition of ZIF−8 (UZ) improved UiO−66 stability, with linker degradation occurring at 491°C (27% loss), followed by a sharp drop of approximately 40% at 610°C, associated with ZIF−8 structural breakdown. On the other hand, the UiO−66-free ZZ composite exhibits distinct thermal behavior, with relatively stable weight between 60°C and 250°C, followed by two significant weight-loss steps at approximately 300°C and 470°C, corresponding to the decomposition of the ZIF−67 and ZIF−8 crystalline structures, respectively. The composite structure likely promotes localized degradation, resulting in distinct, separate weight losses consistent with the known thermal profiles of pure ZIF−67 and ZIF−8. [41]. The additional UiO−66 in the ZUZ composite exhibits three distinct thermal decomposition regions, with a weight loss of approximately 13% at 150°C, corresponding to the presence of occluded methanol and water molecules. Likewise, 18% established at 520°C correlates with the structural decomposition of ZIF−67 and UiO−66, and ZIF−8 was decomposed by 52% at 607°C [18]. Notably, ZUZ exhibits outstanding thermal stability, attributed to surface ZIFs that confer enhanced thermal resistance to the composite material [21].

The FTIR spectra of the synthesized MOF composites are presented in Fig. 4**.a and b**. The FTIR spectrum of ZIF−8, presented in Fig. 4**.a,** exhibits distinct absorption bands in the range of 3455–699 $cm^{-1}$. The peaks observed at 3144 $cm^{-1}$ and 2934 $cm^{-1}$ correspond to the asymmetric stretching vibrations of aromatic and aliphatic C-H groups, respectively. Furthermore, the absorption bands between 1300 and 1460 $cm^{-1}$ are attributed to ring-stretching modes. The characteristic peaks at 999 $cm^{-1}$ and 755 $cm^{-1}$ are assigned to C-N bending vibrations and C-H bending modes, respectively [42].

In Fig. 4**.b**, the red curve representing the UiO−66 spectrum displays broad absorption bands centered at 3419 $cm^{-1}$, suggesting the presence of hydroxyl groups (-OH) on the external surface. Additionally, the carboxylate functionality of the BDC ligand is characterized by two distinct peaks: a symmetric O-C-O stretching at 1398 $cm^{-1}$ and an asymmetric O-C-O stretching at 1586 $cm^{-1}$. The minor absorption band at 1504 $cm^{-1}$ corresponds to C═C stretching vibrations within the aromatic ring of the BDC ligand. The characteristic signal at 1660 $cm^{-1}$ is assigned to C═O stretching vibrations in carboxylic acid moieties, potentially indicating the presence of defects within the cluster [43]. The absorption bands at 660 $cm^{-1}$ and 748 $cm^{-1}$ are attributed to $\mu$ 3-O stretching which is associated with Zr-(OC) coordination [44]. The composite materials UZ and ZUZ demonstrate spectral features characteristic of both constituent components (ZIF−8 and UiO−66), with ZUZ exhibiting enhanced intensity of 2-methylimidazole vibrational modes due to additional ZIF−67 incorporation. By contrast, the ZZ composite exhibits a notable absence of UiO−66 spectral features and closely aligns

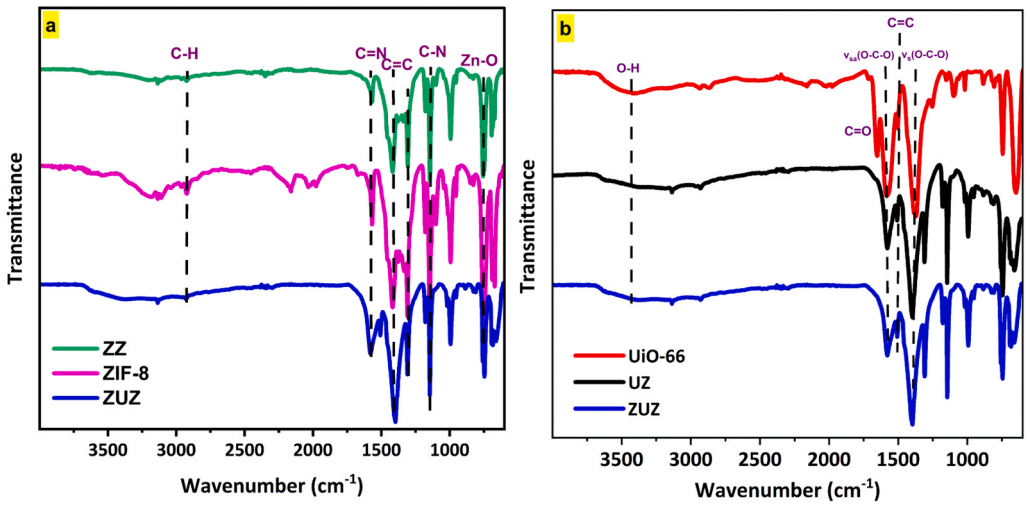


**Fig. 4.** Comparative FTIR spectra of the synthesized MOF composites: (a) ZUZ, ZZ, and ZIF−8, and (b) ZUZ, UZ, and UiO−66, highlighting characteristic functional groups and framework interactions.

with the absorption patterns of ZIF−8 and ZIF−67. These spectroscopic findings offer definitive confirmation of the successful synthesis and structural integrity of all composite materials [36], [45].

The TEM images presented in Fig. 5 provide detailed morphological information about the synthesized MOFs, revealing structural distinctions among ZZ, UZ, and ZUZ. The UiO−66 sample, shown in Fig. 5**.a-b** (UiO−66), displays an amorphous morphology composed of agglomerated nanoparticles with a diameter of approximately 100 nm. In contrast, the addition of ZIF−8 to form the UZ composite results in two separate phases, with ZIF−8 forming large polyhedral crystals of about 500 nm, as visualized in Fig. 5**. c-d**. Furthermore, as shown in Fig. 5**.e-f**, ZZ exhibits nanorod-like structures with widths ranging from 100 nm to 200 nm and lengths ranging from 200 nm to 800 nm. The absence of distinct polyhedral shapes indicates uncontrolled nucleation and disordered growth, resulting in a different composite. This suggests the creation of an anisotropic effect during the synthesis that caused the nanorod-like morphology. By contrast, the ZUZ composites are a combination of UiO−66, ZIF−8, and ZIF−67, and, as shown in Fig. 5**.g-h**, consist of small amorphous particles (100 nm) and large polyhedral crystallites (500 nm). Each structure is retained as seen in the UZ sample, but with an increased population of amorphous, rounded particles and fewer polyhedral crystallites [46-48].

The EDS elemental maps illustrate the distribution of chemical elements within the synthesized composite structures shown in Fig. 6. **a-c** confirms a uniform distribution of carbon (73.28%), oxygen (21.98%), and zirconium (4.67%) throughout the UiO−66 structure, with negligible presence of other elements (N 0.00%, Zn 0.05%, Co 0.03%). This supports the conclusion that the sample is pure UiO−66, without secondary phases or surface modification. The EDS mapping associated with UZ (Fig. 6**. d-f**) confirms that ZIF−8 is localized in polyhedral particles dominated by both zinc (9.57%) and nitrogen (16.53%). In comparison, zirconium (1.35%) and oxygen (3.92%) are predominantly found in the amorphous structures. The EDS mapping in Fig. 6**. g-i** for the ZZ sample reveals a uniform distribution of nitrogen across the nanorods, with an overall atomic concentration of 21.00%. Notably, zinc exhibits a concentration gradient, with higher levels observed at the center of the nanorods, gradually decreasing towards the edges, resulting in an average concentration of 2.98%. In contrast, cobalt exhibits an inverse distribution, with its concentration (2.51%) predominantly localized at the nanorod edges.

The uneven distribution of Co and Zn indicates phase separation occurred during ZIF−8 and ZIF−67 co-synthesis, Fig. 6**. j-l** the distribution of elements of ZUZ resembles to UZ; oxygen (15.89%) and zirconium (7.61%) are preferentially localized within amorphous regions, whereas zinc (9.52%), cobalt (2.07%), and nitrogen (6.29%) exhibit distribution across both amorphous and polyhedral domains, with zinc showing enhanced concentration in polyhedral crystallites. This suggests that ZIF−8 and UiO−66 are phase-separated, despite being synthesized in situ, whereas ZIF−67 appears to be widely distributed across phases. This elemental analysis indicates that the composite is a mixture of ZIF−8 and UiO−66, with widespread ZIF−67 distribution, supporting the integration of all three MOFs within the ZUZ structure.

### 4.2. Surface area and pore size distribution

The textural properties of the synthesized MOFs and MOF composites were investigated by $N_2$ adsorption-desorption measurements at 77 K, and the corresponding isotherms and BJH pore-size distribution curves are shown in Fig. 7**.a and b**. All materials display a sharp $N_2$ uptake at low relative pressure, indicating the presence of accessible microporosity. This feature is characteristic of MOF structures with narrow pore domains and confirms that the microporous frameworks are largely retained after composite formation. In addition, the gradual uptake observed at higher relative pressures, particularly for the composite samples, suggests the presence of secondary porosity arising from interparticle voids, framework aggregation, or hierarchical pore formation [49] UiO−66 exhibits a BET surface area of 582.84 $m^2.g^{-1}$, a total pore volume of 0.29 $cm^3.g^{-1}$, and an average pore diameter of 3.39 nm, consistent with its cage-like porous architecture composed of octahedral and tetrahedral cavities. This behavior agrees with previous reports showing that UiO−66 maintains a stable microporous framework due to its robust Zr-O coordination bonds [50], Pristine ZIF−8 and ZIF−67 show BET surface areas of 1052.23 and 1186.6 $m^2.g^{-1}$, respectively, confirming the high intrinsic microporosity of the parent ZIF frameworks under identical activation and measurement conditions.

After combining ZIF−8 and ZIF−67, the ZZ composite exhibits a substantially reduced BET surface area of 588.97 $m^2.g^{-1}$compared with the pristine ZIF phases. However, its total pore volume increases to 0.37 $cm^3.g^{-1}$, and its average pore diameter reaches 14.33 nm. This apparent difference indicates that ZZ formation reduces the accessible microporous surface area while generating larger interparticle voids or mesoporous domains. This interpretation is supported by the BJH distribution in Fig. 7**.b**, where ZZ shows a broader contribution across the mesopore region, especially at larger pore diameters. Such behavior is consistent with partial intergrowth and aggregation of ZIF−8/ZIF−67 crystallites, leading to the disordered nanorod-like morphology observed by TEM [51]. The UZ composite shows the highest BET surface area of 1672.52 $m^2.g^{-1}$, along with the largest total pore volume of 0.63 $cm^3.g^{-1}$ and an average pore diameter of 10.78 nm. This considerable increase demonstrates that the incorporation of ZIF−8 onto UiO−66 significantly enhances the accessible porous surface while preserving an open composite architecture. The $N_2$ isotherm of UZ shows the highest overall adsorbed volume among the investigated samples, confirming the strong contribution of accessible ZIF−8 derived porosity. In the BJH plot, however, UZ displays a relatively limited mesopore contribution compared with ZZ suggesting that maybe its high surface area mainly originates from accessible micropore domains rather than broad mesoporosity. This interpretation is consistent with the polyhedral morphology observed by TEM, where ZIF−8 particles coexist with UiO−66 domains without severe morphological disruption [52]. The ternary ZUZ composite exhibits a BET surface area of 1169.79 $m^2.g^{-1}$and a total pore volume of 0.53 $cm^3.g^{-1}$ both higher than those of UiO−66 and ZZ but lower than those of UZ. This indicates that the incorporation of ZIF−67 into the UiO−66/ZIF−8 system modifies the pore architecture rather than simply increasing the surface area. The decrease in BET surface area compared with UZ is maybe resulted from partial limit of micropore accessibility caused by the heterogeneous distribution of the ZIF−67. However, the BJH pore-size distribution shows that ZUZ maintains a moderate pore contribution across the analyzed pore range, indicating preservation of a more interconnected hierarchical pore network. Overall, the combined analysis of Fig. 7**.a and b** demonstrates that the sequential formation of binary and ternary MOF composites strongly modifies the accessible porosity of the parent frameworks. The results show that BET surface area alone does not fully describe the textural properties of these materials. Instead, pore volume, pore-size distribution, interparticle voids, and pore connectivity must also be considered when evaluating the porous architecture. The implications of these textural characteristics for $CO_2$ adsorption behavior are discussed separately in Section 4.3.

### 4.3. $CO_2$ uptake and cycling

Fig. 8**.a** shows the $CO_2$ adsorption isotherms of UiO−66, ZZ, UZ, and ZUZ measured at 303 K over the pressure range of 0–10 bar under pure dry $CO_2$. At 10 bar and 303 K, the adsorption capacities follow the order ZUZ (7.0 mmol.$g^{-1}$) > UZ (5.0 mmol.$g^{-1}$) > UiO−66 (3.2 mmol.$g^{-1}$) > ZZ (2.4 mmol.$g^{-1}$). This trend demonstrates that $CO_2$ adsorption is not governed by BET surface area alone, since UZ exhibits the highest BET surface area and pore volume, whereas ZUZ shows the highest experimental $CO_2$ uptake.

The superior adsorption performance of ZUZ can be better explained by considering the combined effects of pore-size distribution, pore

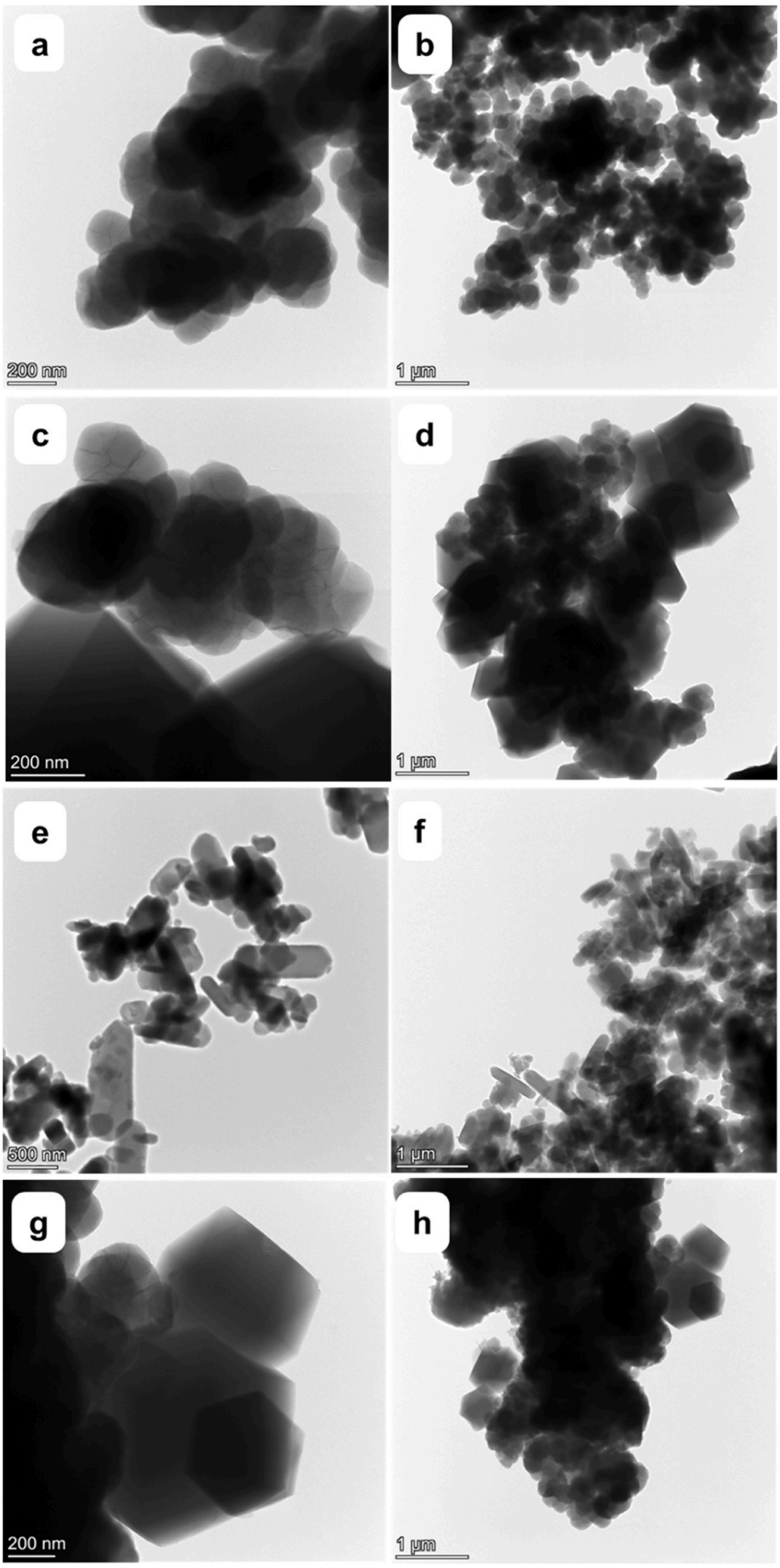


**Fig. 5.** TEM images of the synthesized MOF composites at medium and low magnifications: (a-b) UiO−66, (c-d) UZ, (e-f) ZZ, and (g-h) ZUZ.

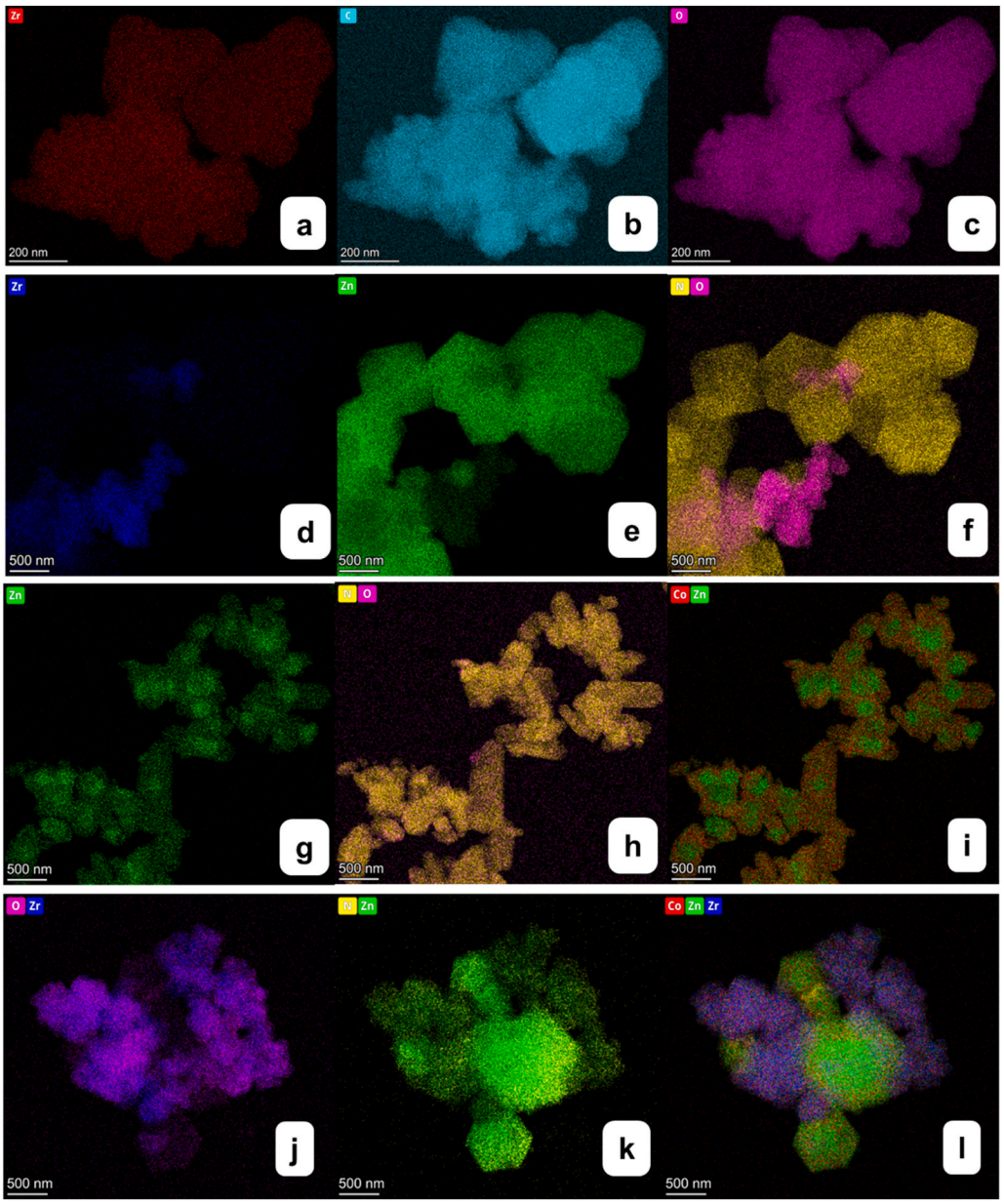


**Fig. 6.** EDS elemental maps of the synthesized MOF composites (a-c) UiO−66, (d-f) UZ, (g-i) ZZ, and (j-l) ZUZ.

accessibility, pore connectivity, and framework chemistry. As shown by the $N_2$ adsorption isotherms and BJH pore-size distribution analysis in Fig. 7**.a and b**, UZ possesses the highest surface area and total pore volume, but its pore size distribution indicates a relatively limited contribution from larger pore domains. In contrast, ZUZ maintains a significant pore volume together with a broader and more pore-size distribution, suggesting the presence of interconnected micro and mesoporous domains. Such hierarchical pore architecture is beneficial for $CO_2$ adsorption because small pores help pore-filling interactions, while mesoporous domains and interparticle voids facilitate molecular diffusion and transport at higher pressure [53,54].

These results show greater performance compared to pristine ZIF−8, ZIF−67, and other composite materials. Lamnini et al. [20] reported $CO_2$ adsorption capacities of only 1.2 mmol/g for ZIF−8 and 0.6 mmol/g for ZIF−67 at 10 bar and 303 K, while Nune et al. [55] reported 7.9 mmol/g with nZIF−8 at 30 bar and 298 K through synthesis modifications that enhanced structural integrity and porosity. This highlights the critical influence of synthesis pathways on surface area and pore accessibility. Gebremariam et al. [56] investigated a HKUST−1/ZIF−8 core-shell composite where HKUST−1 alone exhibited 4.1 mmol/g at 1 bar and 298 K, the composite showed reduced uptake (2.9 mmol/g). Interestingly, ZUZ demonstrates synergistic effects that exceed the individual capacities of the MOFs. Additionally, improved $CO_2/N_2$ selectivity in the composite suggests that ZUZ selectivity may exceed that of UiO−66. To better understand the adsorption mechanism experimental isotherm data were analyzed using the Langmuir, Freundlich, and Temkin models (Table 1). The correlation coefficients ($R^2$) for UiO−66 and UZ, the Langmuir model provides an excellent description of the experimental data with $R^2$ values comparable to those obtained from the Freundlich model indicating that $CO_2$ adsorption on these materials is predominantly governed by monolayer adsorption. In contrast, for ZZ and ZUZ, the Freundlich model shows a slightly better fitting quality than the Langmuir model, with $R^2 > 99\%$ revealing that adsorption on these materials occurs on heterogeneous surfaces with a possible multilayer formation. The fact that both Langmuir and Freundlich fits are close for all samples suggests that the surfaces exhibit mixed behavior, combining both uniform adsorption sites

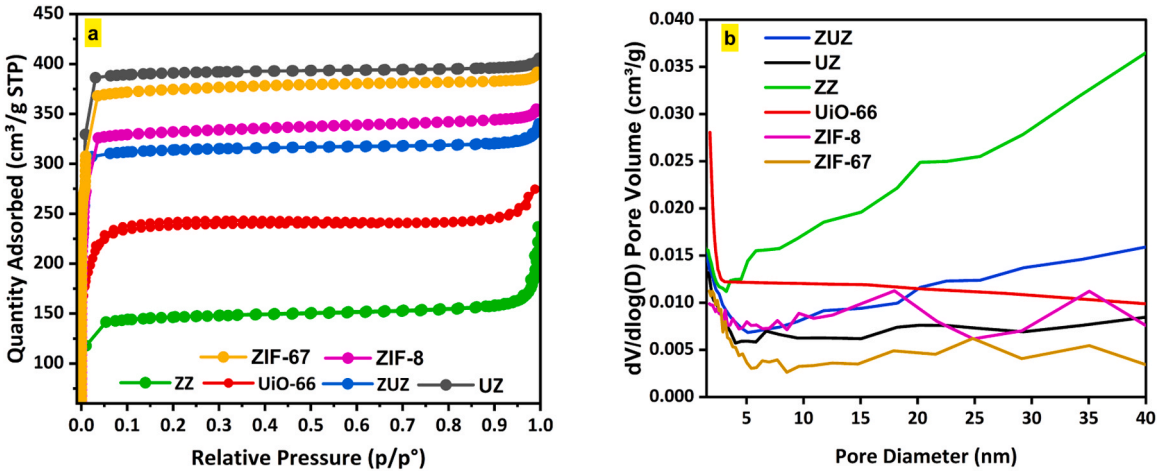


**Fig. 7.** **(a)** Nitrogen adsorption-desorption isotherms at 77 K of UiO−66, ZZ, UZ, ZUZ, ZIF−8, and ZIF−67. **(b)** BJH pore size distribution of all synthesized materials.

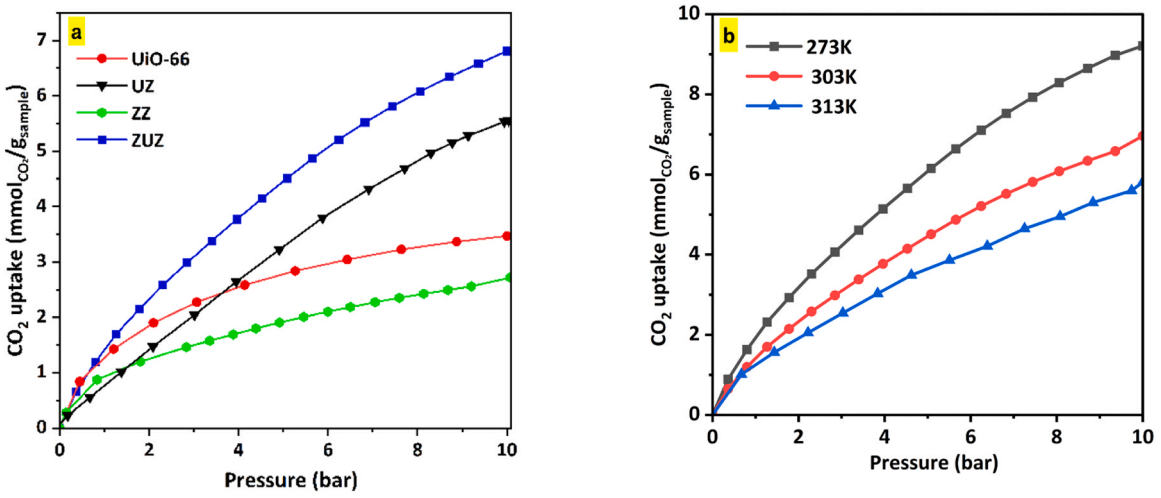


**Fig. 8.** (a) $CO_2$ adsorption isotherms at 303 K of different synthesized MOF composites, illustrating variations in adsorption capacity as a function of pressure. (b) Temperature-dependent $CO_2$ adsorption isotherms of the ZUZ composite, demonstrating the impact of thermal conditions on adsorption performance and equilibrium uptake behavior.

and heterogeneous energetic domains, which is due to the composite MOF [40,57,58]. The Langmuir maximum adsorption capacity $q_m$, follows the order UZ (19.64 mmol/g) > ZUZ (13.41 mmol/g) > UiO−66 (4.26 mmol/g) > ZZ (3.63 mmol/g), confirming that the incorporation of ZIF phases into UiO−66 significantly enhances $CO_2$ uptake capacity. The Temkin heat constant $b_T$, which reflects the strength of $CO_2$ framework interactions, follows the order ZUZ (2.02 J/mol) > UZ (1.52 J/mol) > UiO−66 (0.88 J/mol) > ZZ (0.58 J/mol), indicating that the strongest energetic interactions occur in the ternary composite ZUZ due to the coexistence of multiple metal centers (Zr, Zn, Co). The Freundlich constant, K sub cap F, related to adsorption capacity on heterogeneous surfaces, reaches its highest values for ZUZ (1.49), UiO−66 (1.38), ZZ (0.88), and UZ (0.85), confirming the adsorption ability of ZUZ. Moreover, the heterogeneity index $n$ remains below unity for all materials UZ (0.96), ZUZ (0.69), ZZ (0.52), UiO−66 (0.46), implying favorable adsorption on energetically heterogeneous surfaces without cooperative effects [34,59] ().

The temperature-dependent adsorption data for the ZUZ composite (Fig. 8b), combined with the thermodynamic parameters in Table 2, provide essential insights into the nature of the adsorbent-adsorbate interactions during $CO_2$ adsorption on ZUZ.

Based on these results, the thermodynamic behavior of ZUZ is spontaneous, with $\Delta G^\circ = 1622.64, -992.71$, and $-534.47$ J/mol at 273, 303, and 313 K, respectively. At the same time, the process is

**Table 1**
Comparison of adsorption isotherm parameters and fitting results.

| | Langmuir | | | Freundlich | | | Temkin | | | |
|---|---|---|---|---|---|---|---|---|---|---|
| | $q_m$ (mmol/g) | $K_L$ ($bar^{-1}$) | $R^2$ (%) | 1/n - | $K_F$ (mmol/g·$bar^{-1/n}$) | $R^2$ (%) | B (mmol/g) | $K_T$ ($bar^{-1}$) | $b_t$ (J/mol) | $R^2$ (%) |
| ZUZ | 13.41 | 0.11 | 99.82 | 0.69 | 1.49 | 99.97 | 1247.11 | 2.08 | 2.02 | 93.4 |
| ZZ | 3.63 | 0.24 | 98.48 | 0.51 | 0.88 | 99.84 | 4343.34 | 6.35 | 0.58 | 94.7 |
| UZ | 19.64 | 0.4 | 99.92 | 0.96 | 0.85 | 99.8 | 1652.98 | 2.41 | 1.52 | 98.4 |
| UiO−66 | 4.26 | 0.39 | 99.47 | 0.46 | 1.38 | 99.01 | 2862.66 | 4.71 | 0.88 | 99 |

**Table 2**
Thermodynamic properties for $CO_2$ adsorption on MOFs.

| ΔH° (J/mol) | ΔS° (J/mol. K) | ΔG° (J/mol) | | |
|---|---|---|---|---|
| −1035.9 | −3.07 | **273 K** | **303 K** | **313 K** |
| | | −1622.64 | −992.71 | −534.47 |

exothermic, ΔH° −1035.9 J/mol. It becomes more ordered during adsorption, as shown by the negative entropy change ΔS° = −3.07 J/mol.K. When compared to other materials, ZUZ behaves differently. For NaA zeolite, Jabli et al. [60] reported a exothermic adsorption process with ΔH° = −18.38 kJ/mol and a negative entropy change (ΔS° = −55 J/mol.K) indicating strong $CO_2$ zeolite interactions and a significant ordering of $CO_2$ molecules within the microporous structure. The corresponding ΔG° values range from −4.47 to −1.14 kJ/mol between 253 and 313 K, confirming a spontaneous, weaker adsorption at higher temperatures for functionalized granular activated carbon at 6 bar, as reported by Mashhadimoslem et al. [61] reported ΔH° values of −17.97 kJ/mol for $CO_2$, with ΔG° remaining strongly negative (−7.67 to −6.64 kJ/mol between 298 and 328 K, reflecting spontaneous physisorption. For polymeric ionic adsorbents, Shahrom et al. [34] reported an even higher enthalpy change for vinylbenzyltrimethylammonium arginine (poly[VBTMA][Arg]) ΔH° = −30.3 kJ/mol with a substantial entropy decrease ΔS° = −91.14 J/mol.K highlighting a much stronger and more ordered adsorption mechanism approaching the limit of strong physisorption and corresponding Gibbs free energy changes from −3.16 kJ/mol at 298 K to a value of + 0.27 kJ/mol at 333 K. while, in the temperature swing adsorption study on NiO-supported activated carbon, Lahuri et al. [62] reported values of ΔH° = + 6.61 kJ/mol and ΔG° between −11.56 and −12.75 kJ/mol (303–323 K), suggesting endothermic adsorption governed by surface redox-assisted interactions. Overall, these comparisons show that ZUZ fully behaves as physisorption and is thermodynamically stable, making it a suitable material for low-temperature $CO_2$ capture.

Building on the results from the adsorption isotherms and thermodynamic analyses, which suggested a multilayer adsorption behavior and physisorption mechanism. The cycling performance of the ZUZ composite further confirms its structural reliability and stability under repeated use. As shown in Fig. 9, the ZUZ composite maintained a high and nearly constant $CO_2$ uptake (0.96–0.94 mmol/g) over five consecutive adsorption-desorption cycles, with only minimal loss in capacity observed. This strong maintenance indicates that the adsorption sites remain broadly accessible and that the material is resistant to pore blockage or framework collapse upon regeneration. The regeneration step, conducted thermally at approximately 120 °C, effectively restored the adsorption capacity in each cycle, pointing to reversible interactions between $CO_2$ and the composite surface. Yet, the observed gradual decrease in $CO_2$ uptake across adsorption-desorption cycles is likely attributed to structural or chemical degradation of the adsorbent, pore blockage, or partial loss of active sites. This issue has been reported in thermal cycling in MOFs designed for practical $CO_2$ capture, where structural flexibility and weak bonding environments enable high reuse, but with a possible degradation [63–66]. Therefore, the ZUZ composite demonstrates strong potential for integration into cyclic adsorption systems, offering both high capacity and durability under high regeneration conditions. To further confirm the structural stability of ZUZ under repeated adsorption-desorption conditions, XRD patterns were recorded before and after five $CO_2$ cycling experiments (Fig. 10). All characteristic low-angle diffraction peaks of ZIF−8, ZIF−67, and UiO−66 are retained after cycling, confirming that the bulk crystalline framework remains intact with no evidence of structural collapse or pore destruction. However, a minor peak at approximately 40° 2θ, which may be associated with local short-range ordering of the ZIF−67 surface phase within the composite, disappears after five cycles. Since low-angle peaks reflect long-range structural order while higher-angle reflections are more sensitive to local short-range disorder in ZIF materials [67], this observation may suggest a minor surface-level reorganization of the loosely distributed ZIF−67 phase upon repeated thermal regeneration, which may account for the slight decrease in $CO_2$ uptake capacity observed across cycles (0.96–0.94 mmol/g, 2%), without compromising the overall framework integrity of ZUZ.

The overall findings indicate that composite structuring plays a dominant role in governing $CO_2$ adsorption efficiency. Although the BET surface area is an essential factor, it must be considered alongside pore connectivity, adsorption site distribution, and framework stability. The ZUZ composite effectively combines microporous and mesoporous adsorption mechanisms, optimizing both surface-area-driven multilayer adsorption (as supported by the Freundlich) and energetically favorable

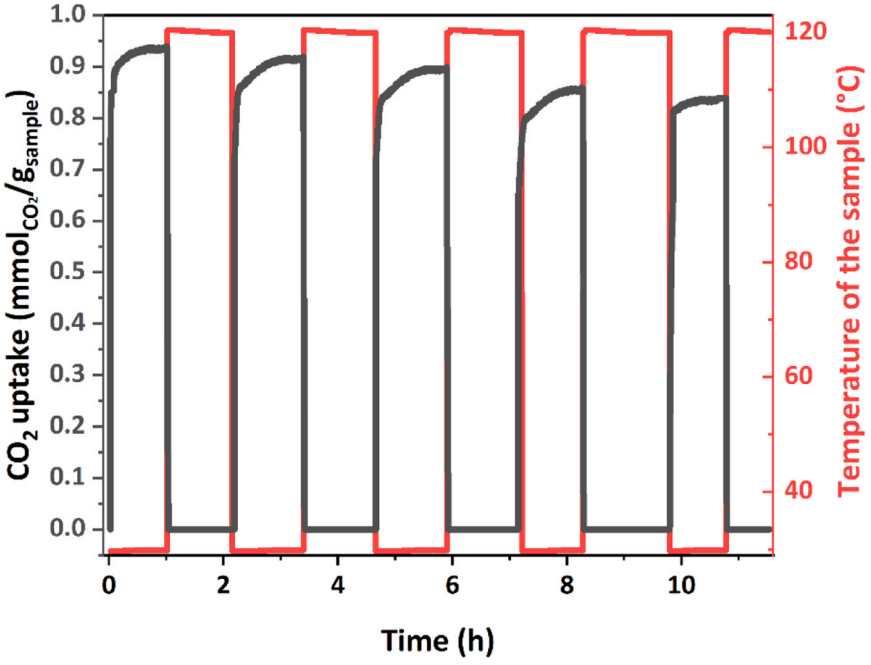


**Fig. 9.** $CO_2$ adsorption-desorption cycling performance of the ZUZ MOF composite over five consecutive cycles.

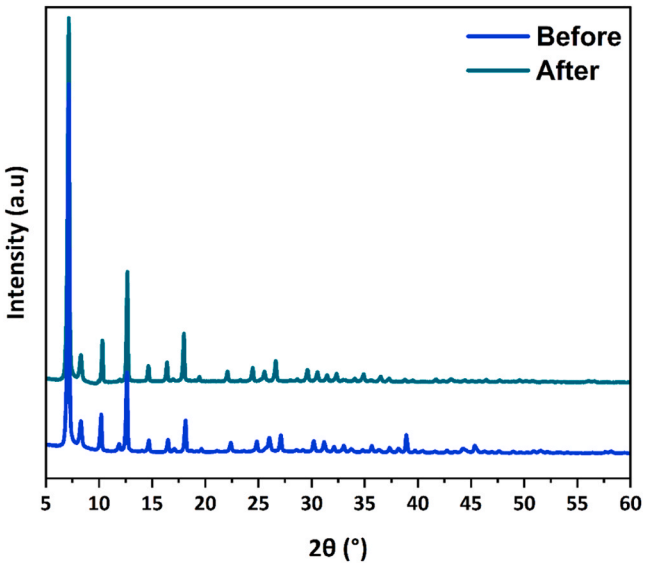


**Fig. 10.** XRD pattens of ZUZ material after five $CO_2$ adsorption-desorption cycling performance.

$CO_2$ binding (as validated by the Temkin model). The enhancement in adsorption behavior aligns with previous studies on hybrid MOFs, such as UiO−66&ZIF−8 composites, which have demonstrated similar improvements in $CO_2$ uptake due to the synergistic effects of different framework structures. Unlike single-phase MOFs, which often suffer from diffusion barriers and limited access to adsorption sites, ZUZ influences the high surface area using ZIF−8 and ZIF−67 while retaining the structural stability by the presence of UiO−66, making it highly suitable for practical $CO_2$ capture. The high-pressure adsorption data obtained in this study (up to 10 bar) are particularly relevant for pre-combustion carbon capture and natural gas sweetening scenarios, where elevated operating pressures are essential to the process. These applications represent industrially significant ways where high-capacity MOF-based adsorbents such as ZUZ could provide practical benefits over conventional materials. It should be noted, however, that the effect of water vapor on $CO_2$ adsorption capacity was not evaluated in this study. Given the hydrophilic nature of UiO−66, competitive water adsorption under humid conditions may reduce $CO_2$ uptake in real flue gas streams that contain moisture. This limitation should be addressed in future work, including comparative experiments under dry and humid conditions to fully assess the practical performance of ZUZ composites. A comparison of the $CO_2$ adsorption performance of various reported composites based on ZIF−8, ZIF−67, or UiO−66 was included in Table 3. By comparing other hybrid composites, ZUZ exhibits the highest $CO_2$ uptake (7.0 mmol/g at 10 bar), despite having a lower surface area than UZ and the composite reported in the literature. This finding supports the idea that ZUZ's superior adsorption capacity is not only dependent on surface area but also on a more favorable pore environment, structural architecture, or stronger host-guest interactions, as suggested by isotherms [68].

## 5. Conclusion

This study clearly demonstrates that mixing UiO−66, ZIF−8, and ZIF−67 plays a key role in changing the textural properties and $CO_2$ adsorption performance of the composites. The ZZ composite exhibits the lowest BET surface area (588.97 $m^2.g^{-1}$) which may be related to morphological changes and alterations in the pore structure during composite formation, which directly limits its $CO_2$ uptake despite the stability and porosity of the individual ZIF phases. Therefore, ZZ shows the weakest adsorption performance among the materials. However, the UZ composite presents a high surface area (1672.52 $m^2.g^{-1}$) and improved structural stability. However, its $CO_2$ adsorption capacity remains moderate, attributed to weaker adsorbate-surface interactions and partial pore blockage, which reduce efficient $CO_2$ diffusion. The ZUZ composite exhibits the best $CO_2$ capture performance, combining a high surface area (1169.79 $m^2.g^{-1}$) with high adsorption capacities of 7.0 mmol/g > UZ (5.0 mmol/g)> UiO−66 (3.2 mmol/g) > ZZ (2.4 mmol/g) at 10 bar and 313 K. This performance is due to the synergistic contribution of the three frameworks, where ZIF−8 enhances microporosity UiO−66 ensures structural stability and ZIF−67 improves morphology. Isotherm analysis further clarifies that UiO−66 and UZ are described effectively by both Langmuir and Freundlich models, whereas ZZ and ZUZ fit the Freundlich model more strongly ($R^2 > 0.99$). The Langmuir maximum capacity $q_m$ follows UZ > ZUZ > UiO−66 > ZZ, while the Temkin constant $b_t$ shows the strongest adsorbate framework interactions in ZUZ due to the coexistence of multiple metal centers. while thermodynamic evaluation reveals a spontaneous, exothermic physisorption process dominated by weak, favorable interactions. Among all prepared materials, ZUZ emerges as the most efficient and balanced CO2 adsorbent, integrating high porosity, optimized chemical functionality, and highlighting the strong potential of designed hybrid

**Table 3**
Comparative table of BET surface area, total pore volume, and average pore size and $CO_2$ uptake for UiO−66, ZZ, UZ, and ZUZ with other composites.

| Samples | BET surface area ($m^2.g^{-1}$) | $V_{tot}$ ($cm^3.g^{-1}$) | $CO_2$ uptake (mmol/g) | | T (K) | Ref |
|---|---|---|---|---|---|---|
| | | | 1 bar | 10 bar | | |
| UiO−66 | 582.84 | 0.29 | 1.20 | 3.2 | 303 | This work |
| ZZ | 588.97 | 0.37 | 0.93 | 2.3 | 303 | This work |
| UZ | 1672.52 | 0.63 | 0.81 | 5.1 | 303 | This work |
| ZUZ | 1169.79 | 0.53 | 1.52 | 7.0 | 303 | This work |
| ZIF−8@Zn-MOF−74 | 633.2 | 0.404 | 0.75 | - | 308 | [69] |
| ZIF−8@ZIF−67 | 1490 | 0.93 | 0.98 | - | 298 | [23] |
| CFAZ/ZIF−8 | 426 | 0.28 | 2.83[a] | - | 298 | [70] |
| PAA@UiO−66 | 445 | 0.41 | 0.74[b] | - | 298 | [71] |
| ZIF−8/GO | 689 | - | 1.19 | - | 298 | [72] |
| ZIF−8 PEI | - | - | 0.91 | - | 303 | [72] |
| ZIF−8 | 1318 | - | 0.75 | - | 303 | [72] |
| ZIF−67@ZIF−8 PLs | 1693.1 | 0.598 | 0.40 | 1.37 | 298 | [73] |
| HKUST−1@ZIF−8 | 806.3 | 0.46 | 2.9 | - | 298 | [74] |
| Mg-MOF−74@ZIF−8–1 | 1423.4 | - | 6.62 | - | 298 | [75] |
| Mg-M OF−74@ZIF−8–2 | 1436.9 | - | 5.09 | - | 298 | [75] |
| Mg-MOF−74@ZIF−8–3 | 1473.8 | - | 4.46 | - | 298 | [75] |

[a] pressure is 0.1 bar.
[b] pressure is 4 bar.

MOF composites for practical carbon capture applications.

## CRediT authorship contribution statement

**Tausif Altamash:** Writing – review & editing, Validation, Supervision, Project administration, Investigation, Data curation. **Zsolt Czigány:** Writing – review & editing, Validation, Investigation, Data curation. **Hicham Akaya:** Writing – original draft, Validation, Software, Methodology, Investigation, Data curation. **Zineb Ouzrour:** Writing – original draft, Validation, Software, Methodology, Investigation, Data curation. **Katalin Balázsi:** Writing – review & editing, Validation, Investigation, Data curation. **Soukaina Lamnini:** Writing – review & editing, Validation, Supervision, Investigation. **Johan Jacquemin:** Writing – review & editing, Visualization, Validation, Supervision, Software, Project administration, Methodology, Funding acquisition, Formal analysis, Data curation, Conceptualization.

## Declaration of Competing Interest

The authors declare that they have no known competing financial interests or personal relationships that could have appeared to influence the work reported in this paper.

## Acknowledgements

This action benefited from the financial support of the Chair "Sustainable Energy," led by Mohammed VI Polytechnic University and sponsored by OCP. This research was also supported by grant no. VEKOP−2.3.3–15–2016–00002 of the European Structural and Investment Funds.

## Appendix A. Supporting information

Supplementary data associated with this article can be found in the online version at doi:10.1016/j.jcou.2026.103516.

## Data availability

Data will be made available on request.

## References

[1] S. Zavahir, et al., Fluorescent Zn(II)-based metal-organic framework: interaction with organic solvents and CO2 and methane capture, Molecules 27 (12) (Jan. 2022) 3845, https://doi.org/10.3390/molecules27123845.
[2] T. Altamash, et al., Carbon dioxide solubility in phosphonium-, ammonium-, sulfonyl-, and pyrrolidinium-based ionic liquids and their mixtures at moderate pressures up to 10 bar, J. Chem. Eng. Data 62 (4) (Apr. 2017) 1310–1317, https://doi.org/10.1021/acs.jced.6b00833.
[3] R. Fourie, H. Hashemi, P. Naidoo, D. Ramjugernath, Advanced amine solvent strategies for efficient CO2 capture in post-combustion systems, Int. J. Environ. Res. 19 (5) (Sep. 2025) 211, https://doi.org/10.1007/s41742-025-00877-6.
[4] H. Akaya, et al., Valorization of moroccan alfa grass through pyrolytic conversion to biochar for atmospheric CO2 capture, ACS Omega 10 (48) (Dec. 2025) 58991–59003, https://doi.org/10.1021/acsomega.5c07867.
[5] J.J. Delgado-Marín, D.P. Izan, M. Molina-Sabio, E.V. Ramos-Fernandez, J. Narciso, New generation of MOF-monoliths based on metal foams, Molecules 27 (6) (Mar. 2022) 1968, https://doi.org/10.3390/molecules27061968.
[6] K. Kalauni, A. Vedrtnam, M. Wdowin, S. Chaturvedi, ZIF for CO2 Capture: Structure, Mechanism, Optimization, and Modeling, Processes 10 (12) (2022), https://doi.org/10.3390/pr10122689.
[7] J. Avila, et al., High-Performance Porous Ionic Liquids for Low-Pressure CO2 Capture**, Angew. Chem. - Int. Ed. 60 (23) (2021) 12876–12882, https://doi.org/10.1002/anie.202100090.
[8] A. Knebel, et al., Solution processable metal–organic frameworks for mixed matrix membranes using porous liquids, Nat. Mater. 19 (12) (Dec. 2020) 1346–1353, https://doi.org/10.1038/s41563-020-0764-y.
[9] W.-L. Xue, et al., Highly porous metal-organic framework liquids and glasses via a solvent-assisted linker exchange strategy of ZIF-8, Nat. Commun. 15 (1) (May 2024) 4420, https://doi.org/10.1038/s41467-024-48703-5.
[10] S. Saghir, et al., Review, recent advancements in zeolitic imidazole frameworks-67 (ZIF-67) and its derivatives for the adsorption of antibiotics, J. Environ. Chem. Eng. 12 (4) (Aug. 2024) 113166, https://doi.org/10.1016/j.jece.2024.113166.
[11] X. Zhao, et al., A polyether amine modified metal organic framework enhanced the CO2 adsorption capacity of room temperature porous liquids, Chem. Commun. 55 (87) (2019) 13179–13182, https://doi.org/10.1039/c9cc07243h.
[12] Z. Ouzrour, et al., HCl-assisted fabrication of metal-organic framework UiO-66(Zr) for affordable gas capture, Mater. Adv. (2025), https://doi.org/10.1039/D5MA00461F.
[13] S. Norouzbahari, Z. Mehri Lighvan, A. Ghadimi, B. Sadatnia, ZIF-8@Zn-MOF-74 core–shell metal–organic framework (MOF) with open metal sites: Synthesis, characterization, and gas adsorption performance, Fuel 339 (May 2023) 127463, https://doi.org/10.1016/J.FUEL.2023.127463.
[14] S.R. Hosseini, M. Omidkhah, Z. Mehri Lighvan, S. Norouzbahari, A. Ghadimi, Synthesis, characterization, and gas adsorption performance of an efficient hierarchical ZIF-11@ZIF-8 core–shell metal–organic framework (MOF), Sep. Purif. Technol. 307 (Feb. 2023) 122679, https://doi.org/10.1016/J.SEPPUR.2022.122679.
[15] Y. Zhang, Y. Li, F. Zhang, Y. Wang, J. Li, J. Yang, Insight into construction and growth process of core-shell KCHA@ZIF-8 composites, Microporous Mesoporous Mater. 373 (Jun. 2024), https://doi.org/10.1016/j.micromeso.2024.113130.
[16] A. Kazemi, F. Moghadaskhou, M.A. Pordsari, F. Manteghi, A. Tadjarodi, A. Ghaemi, Enhanced CO2 capture potential of UiO-66-NH2 synthesized by sonochemical method: experimental findings and performance evaluation, Art. no. 1, Sci. Rep. 13 (1) (Nov. 2023), https://doi.org/10.1038/s41598-023-47221-6.
[17] S. Brunauer, P.H. Emmett, E. Teller, Adsorption of Gases in Multimolecular Layers, J. Am. Chem. Soc. 60 (2) (Feb. 1938) 309–319, https://doi.org/10.1021/ja01269a023.
[18] A. Jrad, et al., Critical Role of Defects in UiO-66 Nanocrystals for Catalysis and Water Remediation, ACS Appl. Nano Mater. 6 (20) (Oct. 2023) 18698–18720, https://doi.org/10.1021/acsanm.3c03787.
[19] Y. Zhang, Y. Jia, M. Li, L. Hou, Influence of the 2-methylimidazole/zinc nitrate hexahydrate molar ratio on the synthesis of zeolitic imidazolate framework-8 crystals at room temperature, Sci. Rep. 8 (1) (Jun. 2018) 9597, https://doi.org/10.1038/s41598-018-28015-7.
[20] S. Lamnini, K. Boukayouht, Z. Ouzrour, S. El Hankari, H. Sehaqui, J. Jacquemin, Fabrication of Highly Efficient ZIF-8@PEI Monoliths for CO 2 Capture Using Phosphorylated Cellulose Nanofiber as a Binder, Langmuir 40 (29) (Jul. 2024) 14964–14977, https://doi.org/10.1021/acs.langmuir.4c01162.
[21] M. Zhang, et al., 3D-agaric like core-shell architecture UiO-66-NH2@ZIF-8 with robust stability for highly efficient REEs recovery, Chem. Eng. J. 386 (Apr. 2020) 124023, https://doi.org/10.1016/j.cej.2020.124023.
[22] I.A. Safo, M. Werheid, a C. Dosche, M. Oezaslan, The role of polyvinylpyrrolidone (PVP) as a capping and structure-directing agent in the formation of Pt nanocubes, Nanoscale Adv. 1 (8) (Aug. 2019) 3095–3106, https://doi.org/10.1039/c9na00186g.
[23] Y. Li, P. Xiang, H. Chen, Y. Zhou, Adsorption performance of one- and two-component anionic dyes using core-shell ZIF-8@ZIF-67, J. Solid. State Chem. 315 (Nov. 2022) 123538, https://doi.org/10.1016/j.jssc.2022.123538.
[24] T. Altamash, et al., Gas solubility and rheological behavior study of betaine and alanine based natural deep eutectic solvents (NADES), J. Mol. Liq. 256 (2018) 286–295, https://doi.org/10.1016/j.molliq.2018.02.049.
[25] AMERICAN SOCIETY FOR TESTING AND MATERIALS, "Standard Practice for Calibration of Temperature Scale for Thermogravimetry 1." AMERICAN SOCIETY FOR TESTING AND MATERIALS, 2023. Accessed: Mar. 09, 2025. [Online]. Available: ⟨https://cdn.standards.iteh.ai/samples/18992/ef812929f6e34eae89e794970b4170ac/ASTM-E1582-93.pdf⟩.
[26] F. Farivar, P. Lay Yap, R.U. Karunagaran, D. Losic, Thermogravimetric Analysis (TGA) of Graphene Materials: Effect of Particle Size of Graphene, Graphene Oxide and Graphite on Thermal Parameters, Art. no. 2, C 7 (2) (Jun. 2021), https://doi.org/10.3390/c7020041.
[27] S. Lamnini, K. Boukayouht, Z. Ouzrour, S. El Hankari, H. Sehaqui, J. Jacquemin, Fabrication of Highly Efficient ZIF-8@PEI Monoliths for CO2 Capture Using Phosphorylated Cellulose Nanofiber as a Binder, Langmuir 40 (29) (Jul. 2024) 14964–14977, https://doi.org/10.1021/acs.langmuir.4c01162.
[28] J.-J. You, et al., A cage-based metal-organic framework with a unique tetrahedral node for size-selective CO2 capture, J. Solid. State Chem. 311 (Jul. 2022) 123140, https://doi.org/10.1016/j.jssc.2022.123140.
[29] J. Rouquerol, et al., Recommendations for the Characterization of Porous Solids, De Gruyter, 1994, https://doi.org/10.1515/iupac.66.0925.
[30] R. Essehli, et al., Single crystal structure, vibrational spectroscopy, gas sorption and antimicrobial properties of a new inorganic acidic diphosphates material (NH4) 2Mg(H2P2O7)2•2H2O, Sci. Rep. 10 (1) (Jun. 2020) 8909, https://doi.org/10.1038/s41598-020-65718-2.
[31] R. Essehli, et al., Efficient crystal structure materials as reactive sorbent for the CO2 and CH4 adsorption and storage, Sci. Rep. 14 (1) (Mar. 2024) 6599, https://doi.org/10.1038/s41598-024-57060-8.
[32] A. Nayak, S. Viegas, H. Dasari, N. Sundarabal, Cu-BDC and Cu2O Derived from Cu-BDC for the Removal and Oxidation of Asphaltenes: A Comparative Study, ACS Omega 7 (39) (Oct. 2022) 34966–34973, https://doi.org/10.1021/acsomega.2c03574.
[33] J.S. Piccin, G.L. Dotto, L.A.A. Pinto, Adsorption isotherms and thermochemical data of FDandC RED N° 40 Binding by chitosan, Braz. J. Chem. Eng. 28 (2) (2011) 295–304, https://doi.org/10.1590/S0104-66322011000200014.
[34] M.S. Raja Shahrom, C.D. Wilfred, F.K. Chong, Thermodynamic and kinetic studies on CO2 capture with Poly[VBTMA][Arg, J. Phys. Chem. Solids 116 (May 2018) 22–29, https://doi.org/10.1016/j.jpcs.2018.01.008.
[35] R.I. Kosheleva, T.D. Karapantsios, M. Kostoglou, A.C. Mitropoulos, Thermodynamic analysis of the effect of rotation on gas adsorption, J. Non-Equilib.

Thermodyn. 48 (4) (Oct. 2023) 403–416, https://doi.org/10.1515/jnet-2022-0086.
[36] D.D. Kachhadiya, Z.V.P. Murthy, Preparation and characterization of ZIF-8 and ZIF-67 incorporated poly(vinylidene fluoride) membranes for pervaporative separation of methanol/water mixtures, Mater. Today Chem. 22 (Dec. 2021) 100591, https://doi.org/10.1016/j.mtchem.2021.100591.
[37] M. Liu, Y. He, T. Sun, L. Zhai, Adsorption Properties of Dyes on UiO–66 and UiO–66-NH2, in: J. Zhang, R. Ruan, M.J.K. Bashir (Eds.), Environmental Pollution Governance and Ecological Remediation Technology, Springer International Publishing, Cham, 2023, pp. 253–260, https://doi.org/10.1007/978-3-031-25284-6_27.
[38] A.M. Aboraia, et al., Structural characterization and optical properties of zeolitic imidazolate frameworks (ZIF-8) for solid-state electronics applications, Opt. Mater. 100 (Feb. 2020) 109648, https://doi.org/10.1016/j.optmat.2019.109648.
[39] M.A. Nazir, et al., Heterointerface engineering of water stable ZIF-8@ZIF-67: Adsorption of rhodamine B from water, Surf. Interfaces 34 (Nov. 2022) 102324, https://doi.org/10.1016/j.surfin.2022.102324.
[40] Q. Yang, et al., Binary metal organic frameworks (UIO-66 and ZIF-67) for adsorptive removal of Sb, J. Nanopart. Res. 24 (8) (Jul. 2022) 158, https://doi.org/10.1007/s11051-022-05531-2.
[41] S.A. Ahmed, D. Bagchi, H.A. Katouah, M.N. Hasan, H.M. Altass, S.K. Pal, Enhanced Water Stability and Photoresponsivity in Metal-Organic Framework (MOF): A Potential Tool to Combat Drug-resistant Bacteria, Sci. Rep. 9 (1) (Dec. 2019) 19372, https://doi.org/10.1038/s41598-019-55542-8.
[42] M. Ahmad, et al., ZIF-8 Vibrational Spectra: Peak Assignments and Defect Signals, ACS Appl. Mater. Interfaces 16 (21) (May 2024) 27887–27897, https://doi.org/10.1021/acsami.4c02396.
[43] H.-G. Kim, K. Choi, K. Lee, S. Lee, K.-W. Jung, J.-W. Choi, Controlling the structural robustness of zirconium-based metal organic frameworks for efficient adsorption on tetracycline antibiotics, Art. no. 13, Water 13 (13) (Jan. 2021), https://doi.org/10.3390/w13131869.
[44] F. Yang, S. Xie, G. Wang, C.W. Yu, H. Liu, Y. Liu, Investigation of a modified metal-organic framework UiO-66 with nanoscale zero-valent iron for removal of uranium (VI) from aqueous solution, Environ. Sci. Pollut. Res. 27 (16) (Jun. 2020) 20246–20258, https://doi.org/10.1007/s11356-020-08381-4.
[45] Mansi, et al., An insight into surface and diffusion characteristics of UiO-66@ZIF-8 core–shell MOF for asymmetric supercapacitors with unprecedented energy density, Adv. Sustain. Syst. 8 (9) (2024) 2400043, https://doi.org/10.1002/adsu.202400043.
[46] T. Bao, Y. Zou, C. Zhang, C. Yu, C. Liu, Morphological anisotropy in metal–organic framework micro/nanostructures, Angew. Chem. Int. Ed. 61 (44) (2022) e202209433, https://doi.org/10.1002/anie.202209433.
[47] B.P. Carpenter, A.R. Talosig, B. Rose, G.D. Palma, J.P. Patterson, Understanding and controlling the nucleation and growth of metal–organic frameworks, Chem. Soc. Rev. 52 (20) (Oct. 2023) 6918–6937, https://doi.org/10.1039/D3CS00312D.
[48] J. Han, et al., Determining factors in the growth of MOF single crystals unveiled by *in situ* interface imaging, Chem 8 (6) (Jun. 2022) 1637–1657, https://doi.org/10.1016/j.chempr.2022.03.006.
[49] D. Behera, P. Priyadarshini, K. Parida, ZIF-8 metal–organic frameworks and their hybrid materials: emerging photocatalysts for energy and environmental applications, Dalton Trans. 54 (7) (2025) 2681–2708, https://doi.org/10.1039/D4DT02662D.
[50] J. Senith Ravishan Fernando, S.S. Asaithambi, S. Maruti Chavan, Amino-Functionalizing Ce-Based MOF UiO-66 for Enhanced CO2 Adsorption and Selectivity, ChemPlusChem 89 (11) (2024) e202400107, https://doi.org/10.1002/cplu.202400107.
[51] E. Hunter-Sellars, P.A. Saenz-Cavazos, A.R. Houghton, S.R. McIntyre, I.P. Parkin, D.R. Williams, Sol–Gel Synthesis of High-Density Zeolitic Imidazolate Framework Monoliths via Ligand Assisted Methods: Exceptional Porosity, Hydrophobicity, and Applications in Vapor Adsorption, Adv. Funct. Mater. 31 (5) (2021) 2008357, https://doi.org/10.1002/adfm.202008357.
[52] J. Łuczak, M. Kroczewska, M. Baluk, J. Sowik, P. Mazierski, A. Zaleska-Medynska, Morphology control through the synthesis of metal-organic frameworks, Adv. Colloid Interface Sci. 314 (Apr. 2023) 102864, https://doi.org/10.1016/j.cis.2023.102864.
[53] D. Schneider, D. Mehlhorn, P. Zeigermann, J. Kärger, R. Valiullin, Transport properties of hierarchical micro–mesoporous materials, Chem. Soc. Rev. 45 (12) (Jun. 2016) 3439–3467, https://doi.org/10.1039/C5CS00715A.
[54] Y.W. Abraha, C.-W. Tsai, J.W.H. Niemantsverdriet, E.H.G. Langner, Optimized CO2 Capture of the Zeolitic Imidazolate Framework ZIF-8 Modified by Solvent-Assisted Ligand Exchange, ACS Omega 6 (34) (Aug. 2021) 21850–21860, https://doi.org/10.1021/acsomega.1c01130.
[55] S.K. Nune, P.K. Thallapally, A. Dohnalkova, C. Wang, J. Liu, G.J. Exarhos, Synthesis and properties of nano zeolitic imidazolate frameworks, Chem. Commun. 46 (27) (Jun. 2010) 4878–4880, https://doi.org/10.1039/C002088E.
[56] S.K. Gebremariam, et al., MOF@MOF core-shell hybrid adsorbents with controlled water vapor affinity towards enhanced and steady CO2 capture in moist conditions, Carbon Capture Sci. & Technol. 14 (Mar. 2025) 100356, https://doi.org/10.1016/j.ccst.2024.100356.
[57] Z. Mehri Lighvan, S.R. Hosseini, S. Norouzbahari, B. Sadatnia, A. Ghadimi, Synthesis, characterization, and selective gas adsorption performance of hybrid NH2-MIL-101(Fe)/ZIF-8 metal organic framework (MOF), Fuel 351 (Nov. 2023) 128991, https://doi.org/10.1016/j.fuel.2023.128991.
[58] H. Zhang, X. Shi, J. Li, P. Kumar, B. Liu, Selective Dye Adsorption by Zeolitic Imidazolate Framework-8 Loaded UiO-66-NH2, Art. no. 9, Nanomaterials 9 (9) (Sep. 2019), https://doi.org/10.3390/nano9091283.
[59] Y. Cao, et al., Hierarchical Pore Engineering in Al2O3/UiO-66 Nanoarchitectures Synergistic Enhancement for Superior Phosphate Capture From Water (vol. n/a, no. n/a, p), Chem. Asian J. (2025) e00976, https://doi.org/10.1002/asia.202500976.
[60] N. Jabli, Z. Ouzrour, A. Mellalou, J. Jacquemin, Y. Tamraoui, F. Ghamouss, Enhanced CO2 adsorption in synthesized cube-shaped zeolitic 4A framework, Solid. State Sci. 168 (Oct. 2025) 108034, https://doi.org/10.1016/j.solidstatesciences.2025.108034.
[61] H. Mashhadimoslem, M. Safarzadeh Khosrowshahi, M. Jafari, A. Ghaemi, A. Maleki, Adsorption Equilibrium, Thermodynamic, and Kinetic Study of $O_2$ /$N_2$ /$CO_2$ on Functionalized Granular Activated Carbon, ACS Omega 7 (22) (Jun. 2022) 18409–18426, https://doi.org/10.1021/acsomega.2c00673.
[62] "Kinetics and Thermodynamic Modeling for CO2 Capture Using NiO Supported Activated Carbon by Temperature Swing Adsorption," *Biointerface Res Appl Chem*, vol. 12, no. 3, pp. 4200–4219, Aug. 2021, doi: 10.33263/BRIAC123.42004219.
[63] D. Britt, H. Furukawa, B. Wang, T.G. Glover, O.M. Yaghi, Highly efficient separation of carbon dioxide by a metal-organic framework replete with open metal sites, Proc. Natl. Acad. Sci. 106 (49) (Dec. 2009) 20637–20640, https://doi.org/10.1073/pnas.0909718106.
[64] J.-B. Lin, et al., A scalable metal-organic framework as a durable physisorbent for carbon dioxide capture, Science 374 (6574) (Dec. 2021) 1464–1469, https://doi.org/10.1126/science.abi7281.
[65] H. Mahdavi, et al., Engineering insights into tailored metal–organic frameworks for CO2 capture in industrial processes, Langmuir 40 (33) (Aug. 2024) 17387–17395, https://doi.org/10.1021/acs.langmuir.4c01500.
[66] Q. Wang, et al., CO2 capture from high-humidity flue gas using a stable metal–organic framework, Molecules 27 (17) (Aug. 2022) 5608, https://doi.org/10.3390/molecules27175608.
[67] X. Yang, J. Gu, C. Liu, Z. Bai, L. Yang, Partial deligandation activated ZIF-67 for efficient electrocatalytic oxygen reduction reaction, Front. Chem. 10 (Oct. 2022), https://doi.org/10.3389/fchem.2022.983549.
[68] S. Singh, N. Sivaram, B. Nath, N.A. Khan, J. Singh, P.C. Ramamurthy, Metal organic frameworks for wastewater treatment, renewable energy and circular economy contributions, npj Clean. Water 7 (1) (Nov. 2024) 1–22, https://doi.org/10.1038/s41545-024-00408-4.
[69] S. Norouzbahari, Z. Mehri Lighvan, A. Ghadimi, B. Sadatnia, ZIF-8@Zn-MOF-74 core–shell metal–organic framework (MOF) with open metal sites: synthesis, characterization, and gas adsorption performance, Fuel 339 (May 2023) 127463, https://doi.org/10.1016/j.fuel.2023.127463.
[70] R. Aniruddha, I. Sreedhar, Process optimization for enhanced carbon capture and cyclic stability using adsorbents derived from coal fly ash, Environ. Sci. Pollut. Res. 30 (4) (2021) 8393–8402, https://doi.org/10.1007/s11356-021-17453-y.
[71] Y. Chang, H. Huang, L. Wang, Y. Li, C. Zhong, Synergistic dual-Li+ sites for CO2 separation in metal-organic framework composites, Chem. Eng. J. 402 (Dec. 2020) 126201, https://doi.org/10.1016/j.cej.2020.126201.
[72] N. Bhoria, J. Pokhrel, S. Anastasiou, K. Suresh Kumar Reddy, G. Romanos, G. N. Karanikolos, Composite porous nanostructures as multi-action adsorbents and membrane fillers for carbon dioxide separation: Comparative performance of metal organic framework – graphene oxide hybrids, Mater. Today. Proc. 37 (Jan. 2021) 4044–4048, https://doi.org/10.1016/j.matpr.2020.07.466.
[73] J. Li, et al., Porous liquids based on ZIF-67@ZIF-8 through the strategy of interface layer reconstruction for CO2 selective sorption, Chem. Eng. J. 500 (Nov. 2024) 156655, https://doi.org/10.1016/j.cej.2024.156655.
[74] S.K. Gebremariam, et al., MOF@MOF core-shell hybrid adsorbents with controlled water vapor affinity towards enhanced and steady CO2 capture in moist conditions, Carbon Capture Sci. & Technol. 14 (Mar. 2025) 100356, https://doi.org/10.1016/j.ccst.2024.100356.
[75] Y. Wan, et al., Enhancing hydrophobicity via core–shell metal organic frameworks for high-humidity flue gas CO2 capture, Chin. J. Chem. Eng. 61 (Sep. 2023) 82–89, https://doi.org/10.1016/j.cjche.2023.03.002.